Piezoelectric nanoribbons for monitoring cellular deformations

Thanh D. Nguyen[1], Nikhil Deshmukh[2], John M. Nagarah[3], Tal Kramer[2], Prashant K. Purohit[4], Michael J. Berry[2] and Michael C. McAlpine[1]*

Methods for probing mechanical responses of mammalian cells to electrical excitations can improve our understanding of cellular physiology and function[1-3]. The electrical response of neuronal cells to applied voltages has been studied in detail[4], but less is known about their mechanical response to electrical excitations. Studies using atomic force microscopes (AFMs) have shown that mammalian cells exhibit voltage-induced mechanical deflections at nanometre scales[5,6], but AFM measurements can be invasive and difficult to multiplex. Here we show that mechanical deformations of neuronal cells in response to electrical excitations can be measured using piezoelectric $PbZr_xTi_{1-x}O_3$ (PZT) nanoribbons, and we find that cells deflect by 1 nm when 120 mV is applied to the cell membrane. The measured cellular forces agree with a theoretical model in which depolarization caused by an applied voltage induces a change in membrane tension, which results in the cell altering its radius so that the pressure remains constant across the membrane[5,7]. We also transfer arrays of PZT nanoribbons onto a silicone elastomer and measure mechanical deformations on a cow lung that mimic respiration. The PZT nanoribbons offer a minimally-invasive and scalable platform for electromechanical biosensing.

Mechanical interactions are fundamental to cellular biology and physiology. For example, structural remodelling of neuronal cells and synapse formation depend on mechanical processes such as axonal and dendritic elongation[8]. Mechanical tension in the cell membrane plays a key role in axonal development, and mechanical stimulation can profoundly impact nerve regeneration[9]. Notably, numerous studies have shown that there is a measurable volume change that accompanies membrane depolarization or action potentials[10-12]. In particular, swelling on the order of several nanometres has been measured in mammalian neurohypophysis[6] and HEK293 cells[5] using atomic force microscopy (AFM). This voltage-induced membrane deformation is a universal property[5,13] resulting from changes in membrane tension that can be explained by thermodynamics and basic mechanics.

Mechanical equilibrium in membranes demands that the cellular radius depends on membrane tension[7]. Membrane tension can be dictated by an applied electrostatic potential via the thermodynamic Lippman relation[5]. As a result, applying an inhomogeneous electric field across a bilayer membrane induces changes in curvature, an effect resembling converse flexoelectricity[14-16]. Charges on opposing sides of a membrane repel each other laterally, creating a local pressure and changing the net surface tension. Therefore, a modulation in membrane voltage will alter the membrane tension and induce a change in the cellular volume. The magnitude of this effect depends on cellular mechanical properties such as rigidity and elasticity[5,17].

To date, a number of techniques have been developed to interrogate cellular rigidity and cellular mechanical interactions, such as optical tweezers[16,18,19], magnetic twisting cytometry[20] and elastomeric posts[21]. However, for cells such as neurons, which are small, irregularly shaped and with fragile membranes, tools of commensurate size are required for an effective cellular interface. Nanoelectronic materials such as silicon nanowires and graphene offer attractive building blocks for electrical recording devices from cells and neurons[22,23]. Owing to their small active area, these nanomaterials offer exceptional sensitivity and resolution in minimally invasive measurements on the electrical activities of cells. However, these nanosensors have not been used to probe mechanical deformations of cells, although some intriguing studies hint at developments in this regard[24,25]. AFM is still the most commonly used tool for quantification of cellular deformation, despite its complexity and invasiveness.

High-performance piezoelectric $PbZr_xTi_{1-x}O_3$ (PZT) nanomaterials—with charge constants up to 140 pm V^{-1} (refs 26–28)—can enable new electromechanical interfaces for probing small voltage-induced cellular deflections. Here, we designed and fabricated PZT nanoribbons to maximize the electromechanical response to small cellular deflections, and to allow for simultaneous imaging and patch-clamp recording. A schematic of the experimental design is outlined in Fig. 1a, and shows several key features. First, PZT nanoribbons are suspended over a trench as nanobeams to maximize deflection (Fig. 1b, Methods). Second, the use of an underlying substrate of transparent MgO (ref. 27) as well as transparent indium tin oxide (ITO) electrodes facilitates backside chip visualization during electrophysiology measurements. The electrodes are electrically isolated by a coating of SiN_x to ensure no cross-signal response when the chip is placed into solution (Supplementary Fig. S1). For the present study we used PC12 cells, a rat pheochromocytoma cell line that acquires many of the characteristics of sympathetic neurons when treated with nerve growth factor (NGF)[29]. PC12 cells were cultured on the PZT chip, and those cells located on the nanobeam arrays were patch-clamped with a standard glass electrode for membrane voltage stimulation. Figure 1c shows a cultured PC12 cell that developed morphologically normal neurites directly on the PZT array (see Methods).

A key concern is whether PZT nanoribbons can support healthy cellular growth. We rigorously tested the biocompatibility of the PZT sensor chip by performing phase-contrast optical imaging, viability assay tests and electrophysiology experiments. Figure 2a presents optical micrographs that show viable NGF-treated PC12 cells with extensive neurites that have been cultured on a standard

[1]Department of Mechanical and Aerospace Engineering, Princeton University, Princeton, New Jersey 08544, USA, [2]Department of Molecular Biology, Princeton University, Princeton, New Jersey 08544, USA, [3]Broad Fellows Program, Division of Biology, California Institute of Technology, Pasadena, California 91125, USA, [4]Department of Mechanical Engineering and Applied Mechanics, University of Pennsylvania, Philadelphia, Pennsylvania 19104, USA. *e-mail: mcm@princeton.edu

Q1

Q2

Q3

1
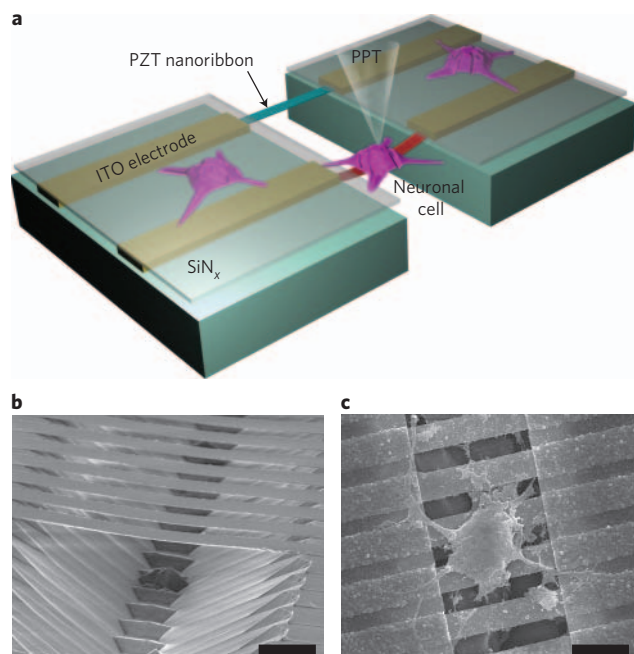
Figure 1 | Interfacing of PZT nanoribbons with cultured neuronal cells.
a, Schematic of the piezoelectric nanoribbon device with cultured neuronal cells. The suspended nanoribbons record cellular mechanical deflections while the glass pipette (PPT) applies and records membrane potentials. **b**, SEM image of suspended PZT nanoribbons (scale bar, 5 μm). **c**, SEM image of a single PC12 cell directly interfaced with suspended PZT nanoribbons (scale bar, 15 μm).
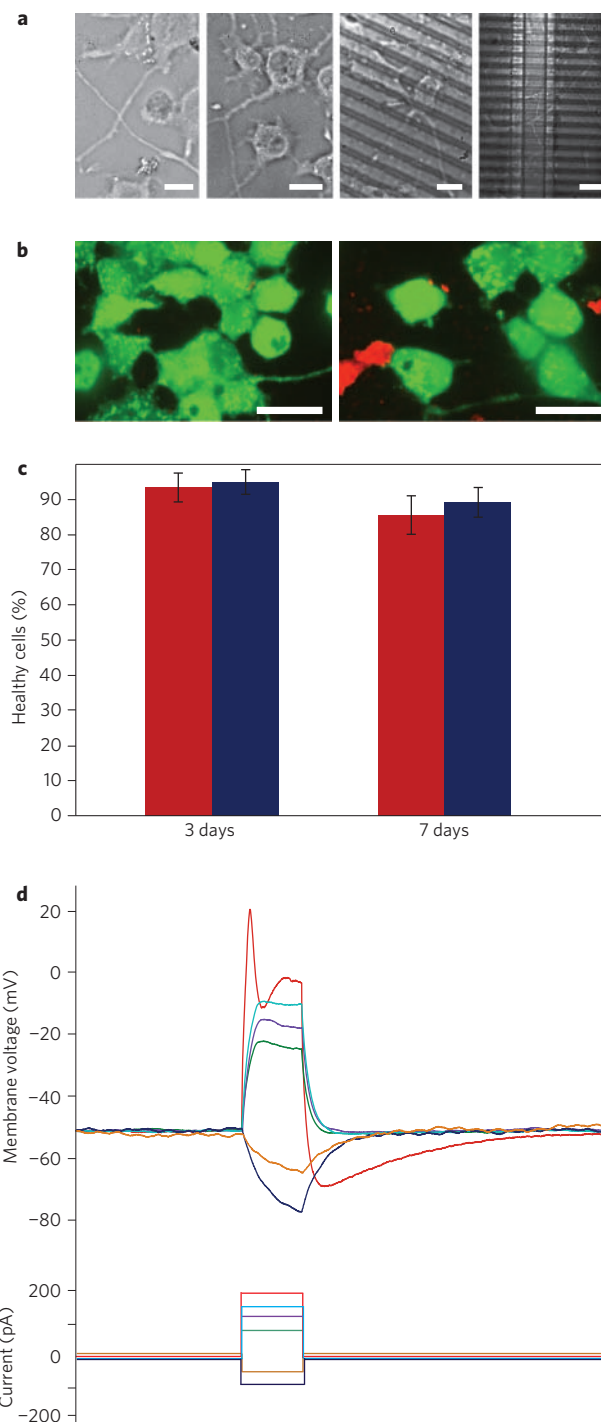
Figure 2 | Biocompatibility of PZT nanoribbons with neuron-like cells.
a, Phase-contrast images of healthy PC12 cells cultured on a standard cell culture dish, on a PZT surface, on PZT nanoribbons and on PZT nanobeams (left to right). Scale bars, 20 μm. **b**, Live/dead viability assay showing live (green) and dead (red) cells on PZT nanoribbons. Cells were cultured for 3 days (left) and 7 days (right). Scale bars, 30 μm. **c**, Percentage of healthy cells cultured on PZT nanoribbons (red columns) compared to cells cultured on a standard culture dish (blue columns) after 3 and 7 days. **d**, A typical electrophysiological voltage response (top) from the membranes of PC12 cells cultured on PZT nanoribbons when current pulses (bottom) are injected in current-clamp mode. The membrane voltage traces are triggered by the current pulse of the same colour. Each of the colours therefore represents a stimulated current and its corresponding membrane voltage.

culture dish, on a PZT surface, on PZT nanoribbons and on suspended PZT nanobeams (left to right). Molecular probes including calcein AM and an ethidium homodimer were used to identify healthy cells (green fluorescence) and damaged cells (red fluorescence; see Methods), and it was found that the majority of cells grown on the PZT nanoribbons were healthy (Fig. 2b; for additional images see Supplementary Fig. S2). Indeed, more than 95% of cells were viable after 3 days of culture, and 85% after 7 days. As shown in Fig. 2c, no difference is observed between the viability of cells grown on PZT nanoribbons and those grown in standard culture dishes in the same culture medium. In both cases, the number of healthy cells decreased after 7 days as cells began to detach from the chip and dish surfaces. These results were similar when culturing PC12 on PZT thin films.

Finally, we tested the electrophysiological response of cells cultured on PZT nanoribbons using standard current-clamp techniques. As shown in Fig. 2d and Supplementary Fig. S3, the response to injected current is typical for PC12 cells. The injecting current stimulates the membrane voltage to reach a threshold value, thereby triggering a stimulus-evoked action potential (SEAP) in the PC12 cells[19,30]. The results are similar for PC12 cells in standard culture medium. The SEAPs are well developed and have relatively large amplitudes, rapid rise rates and brief durations. This suggests that the PC12 cells have expressed voltage-gated ion channels, and thus exhibit typical electrophysiological behaviour when cultured on PZT nanoribbons. As will be demonstrated below, a key point is that, although these results clearly demonstrate the biocompatibility of the PZT nanoribbons, action potentials are not required for electromechanical responses in cells. These responses are induced via charge redistribution within the cell.

To extract quantitative information about neuronal deflections, the PZT nanobeam response must be fully characterized. Figure 3a presents an experiment in which an AFM was used to apply

minute loads (pN–nN) to the nanoribbons to measure the electrical output (see Methods). In scanning mode, the AFM tip intermittently touches the nanobeams at the centre, inducing a piezoelectric signal from the bending of the PZT nanoribbons (Fig. 3b). Subsequently, the force applied by the AFM tip to the PZT nanobeams can be calculated. The force value is identical to the adhesive force derived from a typical force curve of the tip on a PZT nanobeam (Supplementary Fig. S4). As expected, the PZT nanoribbons produce voltage signals that are directly proportional to the magnitude of applied forces from AFM tips with varying spring constants (Fig. 3c). The voltage–force relationship can then be linearly fit to quantify the sensitivity of the PZT nanobeams. This result allows a precise quantification of cellular forces applied on suspended PZT nanoribbons when the voltage signals are generated by cellular deformation.

To measure the cellular deflections induced by a membrane voltage, we used standard whole-cell patch-clamp techniques to stimulate membrane voltages in PC12 cells while recording the electrical response in PZT nanoribbons (see Methods). The transparent chip allows for visualization and manoeuvring of the pipette to the cell surface (Fig. 4a, inset). A control experiment was performed to verify that there was no crosstalk signal from the conducting electrodes or mechanical fluctuations of the glass pipette during the experiment (Supplementary Fig. S5). Significantly, as shown in Fig. 4a, well-defined PZT signals were captured simultaneously with the stimulated PC12 membrane voltage. High-resolution signals were also recorded from deflections due to spontaneous depolarization in the PC12, as shown in Fig. 4b. (Differences in signal magnitudes between cells located at the nanobeam edges (as in Fig. 4a) and those located at the centre (as in Fig. 4b) are discussed in more detail in the Supplementary Methods.)

Critically, by using the AFM calibration of PZT nanoribbon sensitivities, we can quantitatively relate the change of membrane voltage to the force generated by the cell, as plotted in Fig. 4c (error bars include the errors of the fitting process of the AFM calibration as well as variance in the experimental data). It is observed that a change of 120 mV in the cell membrane voltage induces a force of ~1.6 nN on the suspended PZT nanoribbons. This result can also be used to estimate the membrane deflection. Using beam theory, the deflection can be derived as $x = PL^3/48EI$ where x is the deflection, P the applied force, L the length of the PZT nanobeam, E the elastic modulus of PZT, and I the moment of inertia of the beam. With $P \approx 1.6$ nN, $L \approx 20$ μm, $E \approx 100$ GPa (ref. 31), and beam dimensions of width ≈ 5 μm and thickness = 200 nm, the corresponding deflection is ~1.00 nm. As confirmed by Fig. 1c, it should be noted that the cells with a diameter of 20 μm tend to span two suspended nanoribbons. As a result, this cellular deflection becomes distributed over each ribbon, resulting in a per-nanoribbon deflection of 0.5 nm. This result agrees quite well with those of previous studies[5,6,10,11,32].

Using classical mechanics and a model of voltage-induced membrane movement[5], we propose a theoretical model to calculate the cellular forces exerted on the PZT nanobeams. The key concept of the model is that depolarization induces a change in the membrane tension that in turn alters the cellular radius so as to maintain a constant pressure[7] across the membrane. The system was simplified by assuming that the cell is axisymmetric and sits at the centre of the PZT nanoribbon beam during its excitation. Because the resting diameter of the cell is $2R_0 \approx 20$ μm, but the deflection of the PZT is several nanometres, the deflection of the PZT can be considered negligible in comparison to the deformation of the cell. Therefore, the cells are simply considered to be confined between two flat surfaces representing the patch-clamp pipette on top and the PZT beam below (Fig. 4d). Details of the model are described in the Supplementary Methods (results for pancake-shaped cells and cells that are not at the centre of the nanoribbon are also presented
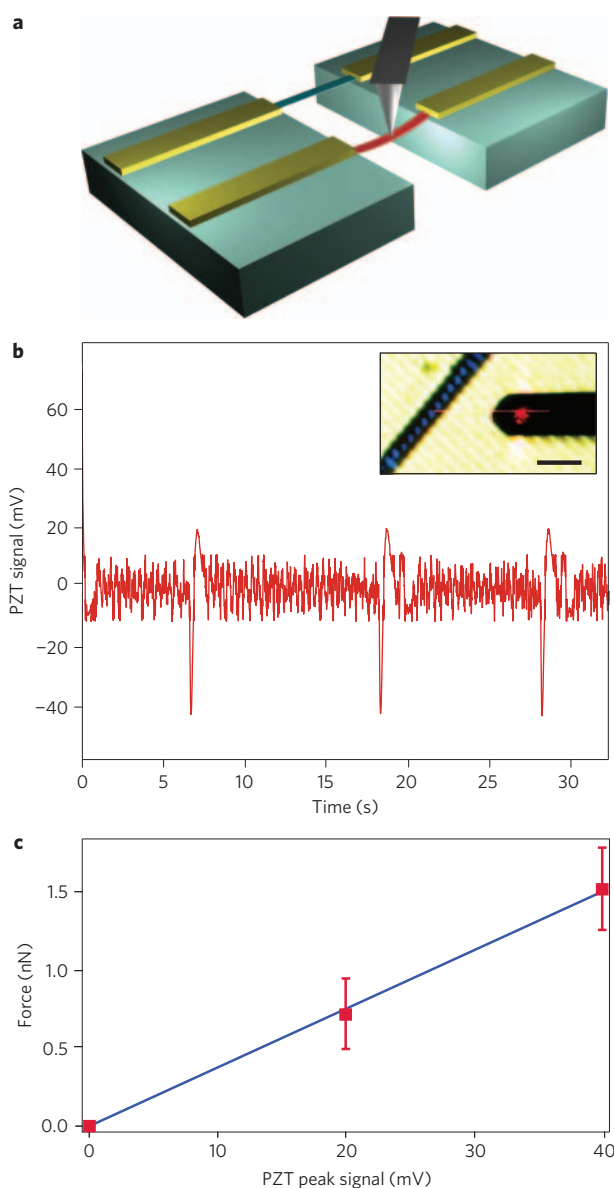
Figure 3 | Quantifying the sensitivity of PZT nanoribbons. a, Schematic showing the experimental set-up. An AFM tip (grey) probes the centre of a PZT nanobeam (red). **b**, Piezoelectric signals generated in response to indentation by the AFM tip during scanning. Inset: tip exerting an indentation force. Scale bar, 50 μm. **c**, Graph showing that the piezoelectric nanoribbon signal depends on the applied force of the AFM tip. The solid line is a fit based on experimental data (points). Error bars arise from the variance in the spring constants of the AFM tips.

there). In brief, the membrane tension τ can be written as

$$
\frac{(\tau - \tau_I)e}{\sqrt{(2k_B T)^2 \varepsilon_0 \varepsilon_W}} = \sqrt{C_{ext}}\left[\sinh^{-1}\left(\frac{q_{ext} - C_m V}{2\sqrt{2c_{ext}k_B T \varepsilon_0 \varepsilon_W}}\right)\right]^2
$$
$$
+ \sqrt{C_{int}}\left[\sinh^{-1}\left(\frac{q_{int} - C_m V}{2\sqrt{2c_{int}k_B T \varepsilon_0 \varepsilon_W}}\right)\right]^2
$$

(1)

where e is electron charge, C_m is the capacitance of the lipid bilayer, V is the change in membrane potential of the cell, and τ_I is a voltage-independent tension. q_{int} and q_{ext} are the charge densities on the interior and exterior leaflets of the cell membrane, ε_W
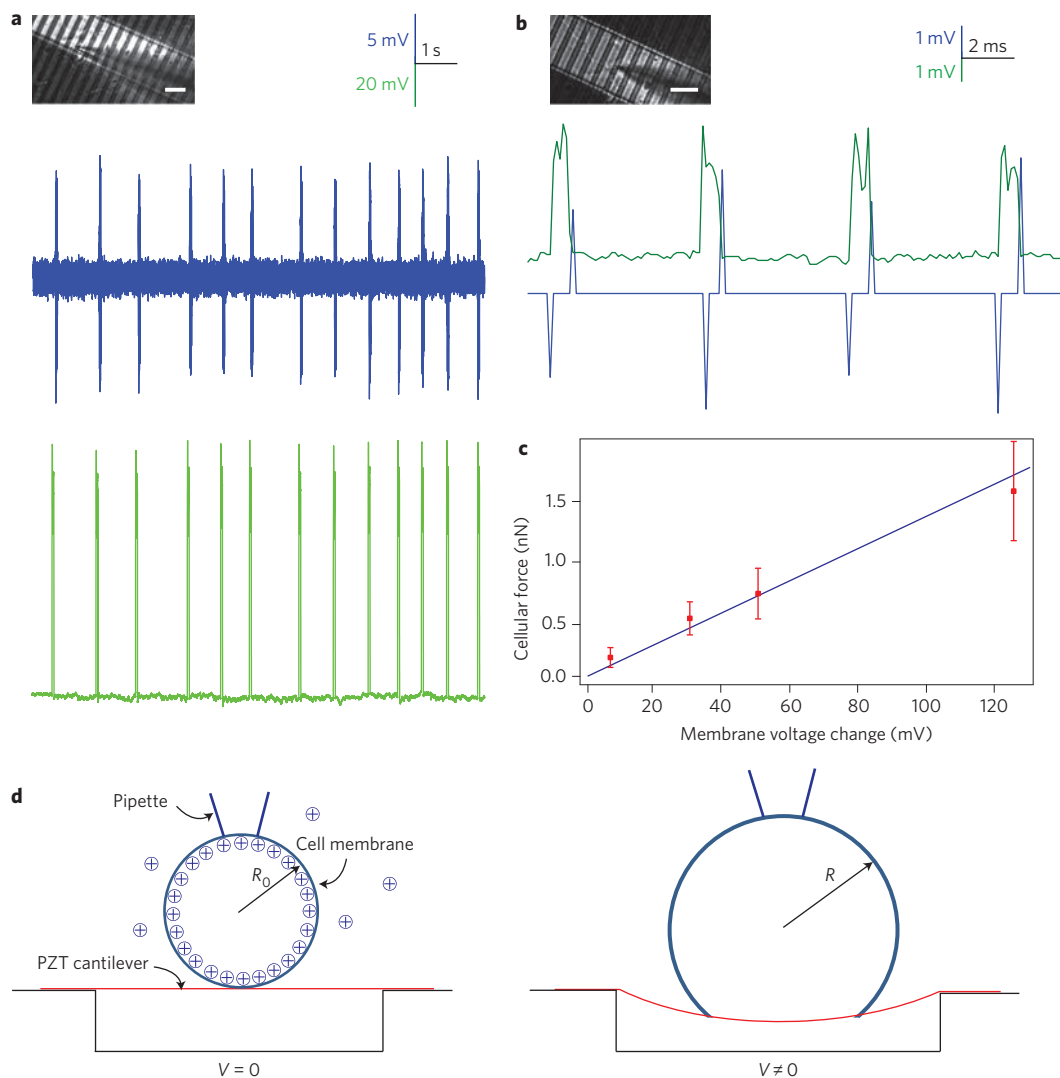
Figure 4 | Probing cellular mechanics using PZT nanoribbons. a, Response of piezoelectric nanoribbons (blue) to cellular deformations evoked by an applied membrane voltage (green). Inset: optical image of the experiment (scale bar, 12 μm). **b,** Response of PZT nanoribbons (blue) to cellular deformations induced by spontaneous depolarization (green). Noise below a threshold of 2.2 mV has been removed for clarity. Inset: the experiment (scale bar, 12 μm). **c,** Relationship between imparted force and membrane potential. Red points represent experimental data. Error bars include errors from the fitting process of the AFM calibration and variance in the experimental data. The solid blue line is a theoretical calculation of the mechanical deformation force. **d,** Schematic of the theoretical model describing the force that the cell (blue circle) exerts on a PZT nanobeam (red line) following electrical excitation from a pipette (blue) on top of the cell. Left panel: the cell in a resting state (applied membrane voltage $V = 0$), with a cellular radius of R_0. Right panel: the cell swells to a radius R in the excited state ($V \neq 0$).

and ε_0 are the relative permittivities of water and vacuum, respectively, c_{ext} and c_{int} are the ionic concentrations on the two sides of the membrane, and $k_B T$ is the thermal energy. The appropriate values for these parameters are available from earlier work[5]. Applying the Young–Laplace law, the cellular force applied on the PZT nanobeam can be written in terms of the cellular radius R as

$$F = \frac{8\pi\tau^2}{\Delta p}\left(1 - \frac{R_0}{R}\right) \qquad (2)$$

where

$$\Delta p = \frac{2\tau_0}{R_0} \qquad (3)$$

and

$$R = \frac{2\tau}{\Delta p} \qquad (4)$$

From equations (1) and (2), we can derive and describe a relationship between the force F and voltage V. This is plotted as the solid blue line in Fig. 4c. Notably, the theoretical result agrees well with the experimental data and provides a thorough understanding of the coupling between electrical and mechanical cellular activities.

Although these results confirm previous studies on cellular electromechanics using techniques such as AFM, there are several key advantages of piezoelectric ribbons. First, AFM makes use of a tip sharpened at the nanometre scale, and thus can be considered invasive. In contrast, PZT nanoribbons are thin and flat and can therefore conform to or even buckle[33,34] onto curvilinear surfaces. Second, AFM is difficult to scale up to multi-tip probing, whereas piezoelectric nanoribbons are made using standard microfabrication techniques and can therefore be scaled easily. Finally, piezoelectric nanoribbons may also be useful in bioelectromechanical energy harvesting applications[28,35], which have no equivalent in scanning probe techniques. As a proof of principle of these concepts, PZT nanoribbons were scaled to macroscopic areas and biointerfaced
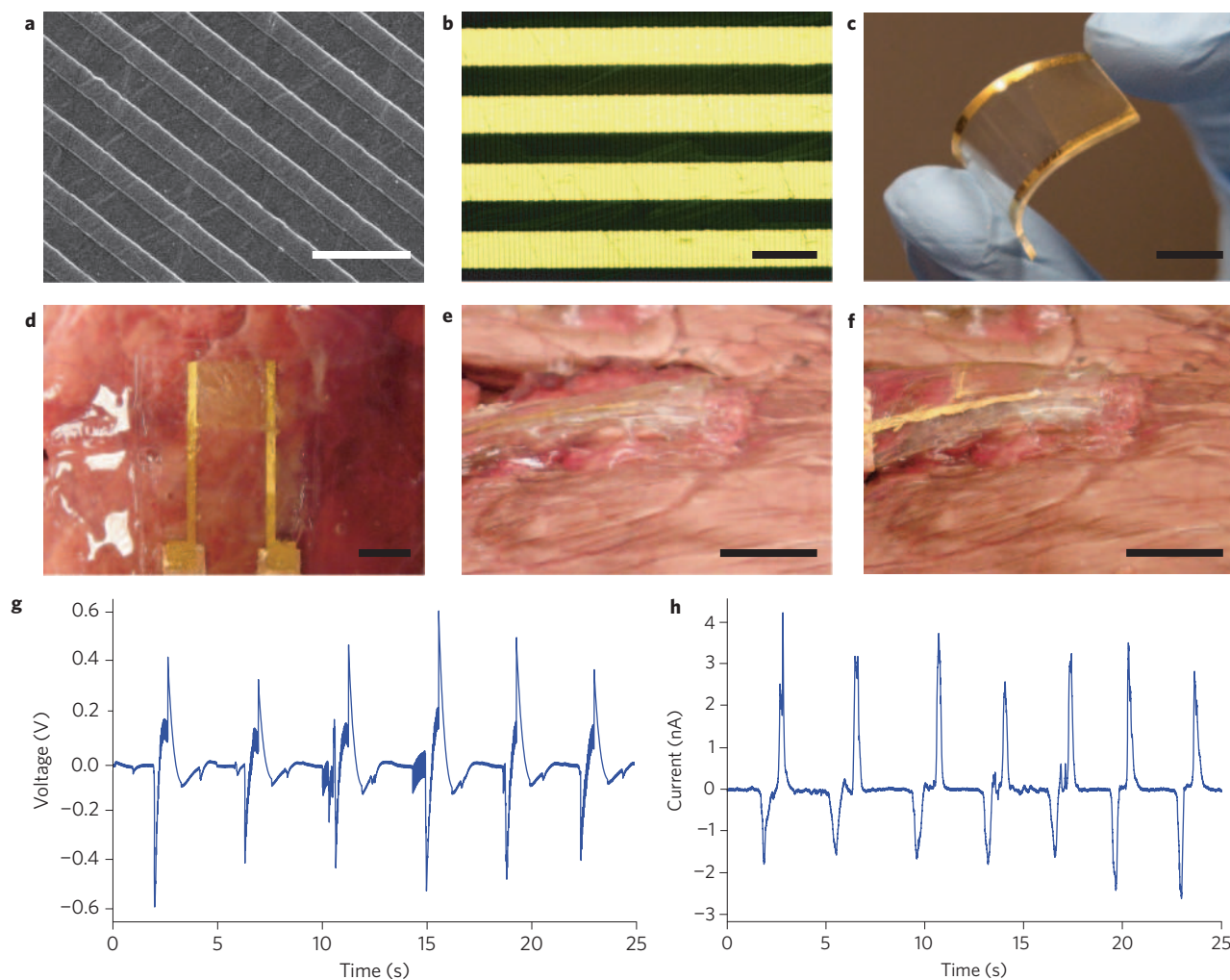
Figure 5 | Biointerfacing of PZT nanoribbons with multicellular cow lung tissue. a, SEM image of PZT nanoribbons following transfer onto a flexible PDMS substrate. Scale bar, 15 μm. **b**, Optical microscope image of PZT nanoribbons (thin vertical lines) and interdigitated gold electrodes (horizontal large yellow lines) on PDMS. Scale bar, 50 μm. **c**, Photograph of flexible PZT nanoribbon chip. **d**, Photograph of PZT nanoribbons on PDMS biointerfaced with cow lung tissue for sensing deformations during a mimicked respiration process. **e**, PZT/PDMS chip at rest on the cow lung. **f**, PZT/PDMS chip in a strained state during the mimicked respiration process. Scale bars, 1 cm (**c**–**f**). PZT voltage (**g**) and current (**h**) signals associated with deformation of the cow lung during the respiration process.   Q15

with the multicellular tissue of an extracted cow lung to mimic the respiration process. PZT nanoribbons were transferred onto the elastomer polydimethylsiloxane (PDMS) using our previously reported method[27,33] (Fig. 5a), contacted with interdigitated gold electrodes (Fig. 5b), and poled in the plane of the ribbons to complete the device, as shown in Fig. 5c (see Methods). The soft, biocompatible device was subsequently biotransferred onto a cow lung to form a direct biointerface between the PZT nanoribbons and the tissue (Fig. 5d). A bicycle pump attached to the lung was then used to simulate mechanical respiration, resulting in periodic strains/deformations in the PZT nanoribbons (Fig. 5e,f and Supplementary Movie S1). This cycled mechanical stimulation led to voltage signals on the order of 0.5 V (Fig. 5g) and currents of several nanoampères (Fig. 5h) from the small strains generated at this intimate biointerface.

In summary, we have demonstrated that PZT nanoribbons represent a unique and novel platform for biomechanical nanosensing. PZT nanoribbons can form a biocompatible interface with cells to act as sensitive extracellular probes to detect minute cellular deformations. Furthermore, these piezoelectric nanoribbons can be biointerfaced directly with tissue for measuring macroscopic electromechanics. Compared to other techniques, the PZT nanoribbons offer multiple advantages, including minimally invasive probing, direct biointerfacing and scalability. Future studies will allow us to extend these results to multiplexed measurements on cellular and neural networks. For example, there is the potential to enhance the sensitivity by reducing the thickness of the PZT nanoribbons, which would increase the deflection resulting from the applied force. We have previously reported a method called PENCiL[26] that allows for the generation of even smaller PZT nanostructures. Sensors making use of smaller PZT nanowires should have the capability to record signals from the smaller structures of cells and neurons, including axons, dendrites and synaptic boutons[6]. Finally, we anticipate that these results will lead to piezoelectric energy harvesting from bioelectromechanical sources[35]. For instance, harvesting the power from lung or diaphragm motion may be useful for providing an alternative power source for implantable biomedical devices.

Methods

Fabrication of PZT nanoribbons. Suspended PZT nanoribbons were fabricated on transparent, double-sided polished single-crystal MgO substrates (MTI Corporation). In a first step, PZT was patterned using lift-off with AZ 5214 photoresist. PZT films (thickness, 200 nm) were then deposited epitaxially using a magnetron sputter at 60 W (radiofrequency) for 5 h and with 25 s.c.c.m. argon flow.   Q9

After lift-off, PZT was post-annealed at 650 °C for 30 min to form a perovskite crystalline structure as previously reported[26,27]. To pattern transparent ITO contact electrodes, a second photolithography step was performed. ITO films (500 nm) were deposited using a magnetron sputter at 100 W (radiofrequency) for 50 min and patterned by lift-off. A passivating SiN$_x$ layer was then deposited by plasma-enhanced chemical vapour deposition (PECVD; 30 min at 250 °C, 900 mtorr, 20 W with 2% SiH$_4$, 150 s.c.c.m. N$_2$ and 2 s.c.c.m. NH$_3$). To suspend the PZT structures, the SiN$_x$ over the PZT was patterned and dry-etched by reactive ion etching (5:50 s.c.c.m. O$_2$:CHF$_3$ at 150 W and 100 mtorr). The chip was then cleaned with O$_2$ plasma (4 min at 90 W and 40 s.c.c.m. O$_2$) to remove residue on the structures. Exposed MgO underneath the PZT was etched away in 85% phosphoric acid at 120 °C for 3 min to undercut the PZT nanobeams. To form a connection with the external electrodes, ITO contact pads at two ends of the chip were opened by dry etching the SiN$_x$. These contact pads were protected from saline solution during experiments by a layer of silicone (Kwik-Cast Sealant, World Precision Instruments). After fabrication, the PZT ribbons were poled by a d.c. voltage of 300 V for 12 h.

PC12 cell culturing on PZT. The rat PC12 cell line[29] was differentiated to sympathetic-type neuronal cultures with nerve growth factor (NGF) in differentiation medium composed of RPMI 1640 medium (Invitrogen) supplemented with 1% horse serum (Invitrogen), and 1% penicillin/streptomycin (Sigma-Aldrich). PC12 cells were exposed to 100 ng ml^{-1} NGF for 10 days before freezing and storage in a primed differentiated state[29]. After fabrication, PZT chips were dipped in 70% ethanol and sterilized in an autoclave for 30 min. Chips were placed in a culture dish before applying silicone to cover the exposed conducting pads. To allow the silicone to dry completely, the culture dishes were kept in a culture hood for 6 h under ultraviolet light. To promote cell adhesion, chips were coated with (10%) poly-L-lysine (Invitrogen) followed by 10 µg ml^{-1} of natural mouse laminin (Invitrogen) diluted in Hanks Balanced Salt Solution (HBSS, Biophysics). The chips were then kept in an incubator at 37 °C overnight and washed twice with 1× HBSS the following day. Primed PC12 cells were thawed rapidly and seeded on the coated chips in differentiation media containing 100 ng ml^{-1} NGF. Cells were incubated in a humidified, CO$_2$-regulated, 37 °C tissue culture incubator for 3–5 days before experimentation. This time period was sufficient to allow for the regeneration of PC12 neurites from a primed culture. For scanning electron microscopy (SEM) imaging, cells were thoroughly washed in deionized water to remove serum in the growth medium and then dipped in 4% formaldehyde for 15 min. After the fixation process, cells were thoroughly washed again with deionized water before staining with 0.1% OsO$_4$. Critical-point drying in CO$_2$ was performed before SEM imaging.

Cell viability tests. PC12 cells were imaged using a phase-contrast optical microscope with water immersion objectives. Viability tests were performed on PC12 cells using test kits from Invitrogen (LIVE/DEAD Viability/Cytotoxicity Kit-L-3224). A two-colour assay of the kit indicated plasma membrane integrity and esterase activity. For staining, the cultured cells were washed with pure RPMI 1640 twice to remove serum medium, soaked in the solution of dyes (2 µM calcein AM and 4 µM ethidium) for 30–40 min, and finally washed with 1× HBSS. A fluorescent confocal microscope (Leica SP5 confocal) was used to image the stained cells. Cells in 15 random fields were imaged and the number of cells displaying green (viable) and red (dead) fluorescence was quantified at 3 and 7 days in culture.

AFM to quantify PZT sensitivity. An AFM Dimension Nanoman (Veeco Instruments) was used to perform force measurements on suspended PZT nanoribbons. Non-conducting AFM tips (undoped silicon, Veeco) with known spring constants (measured via thermal tune) were used to scan and apply different forces on the PZT nanobeams. Forces were calculated based on the force curves in ramping mode. To achieve minute load, the deflection set point was set to zero after engagement. Piezoelectric signals were measured with a nanovoltmeter (Keithley 2182A). The linear fitting and analysis of the dependence of the piezoelectric signal on the applied force was performed by IGOR Pro 6 software (Wavemetrics).

Electrical characterization. Electrophysiological information regarding the cultured PC12 cells was obtained using a whole-cell patch-clamp technique. Recordings were taken from cells cultured on a PZT surface, PZT nanoribbons and a normal culture dish. Glass pipettes with a tip diameter of 1.0 µm were pulled by a pipette puller (P-2000, Sutter Instruments) and fire-polished before measurements. Only PC12 cells that displayed neurites with a resting potential of −30 to −50 mV were used for the experiments. To break into whole-cell mode following gigaohm seal formation, a constant negative pressure was applied and the d.c. voltage was ramped to −500 mV until capacitance transients were seen. Before measurement, the cells were washed three times and then bathed in extracellular recording solution containing 110 mM NaCl, 22 mM NaHCO$_3$, 2.5 mM KCl, 1.6 mM MgCl$_2$, 1 mM CaCl$_2$ and 10 mM D-glucose, and the pH was adjusted to 7.3 with NaHCO$_3$. The composition of the intracellular saline solution was 140 mM KCl, 5 mM KCl, 10 mM HEPES, 1 mM MgCl$_2$, 1 mM CaCl$_2$, pH ∼ 7.3 with NMG-OH. Electrophysiology data were recorded with a two-channel MultiClamp 700B (Axon Instruments) system. Two copper wires from the PZT chip were connected to the second channel of the MultiClamp amplifier to synchronize with the membrane voltage signal from the

first channel. The evoked membrane voltage was stimulated by injecting current in current-clamp mode. Noise below a threshold of 2.2 mV was removed.

PZT nanoribbons biointerfaced with cow lung tissue. PZT nanoribbons were transferred to PDMS (1 mm) as described in our previous reports[27,33]. To fabricate interdigitated electrodes, a photolithography process was performed on the PDMS substrate. Gold/titanium (200 nm/3 nm) was deposited on the PZT nanoribbon/PDMS chip. Photoresist (AZ5214) was then spin-coated and exposed to ultraviolet light to form electrode patterns. Wet-etching for 45 s in gold-etchant (Transene GE-6) was used to etch away exposed gold. Photoresist was finally stripped by flood-exposure under ultraviolet light for 5 min, and dipping in the developer AZ-400 for 30 s. The final chip was biointerfaced with explanted cow lung tissue via direct attachment and using a thin layer of adhesive silicone.

References

1. Arlett, J. L., Myers, E. B. & Roukes, M. L. Comparative advantages of mechanical biosensors. *Nature Nanotech.* **6,** 203–215 (2011).
2. Montell, D. J. Morphogenetic cell movements: diversity from modular mechanical properties. *Science* **322,** 1502–1505 (2008).
3. Vaziri, A. & Gopinath, A. Cell and biomolecular mechanics *in silico*. *Nature Mater.* **7,** 15–23 (2008).
4. Kim, D. H. *et al.* Dissolvable films of silk fibroin for ultrathin conformal bio-integrated electronics. *Nature Mater.* **9,** 511–517 (2010).
5. Zhang, P. C., Keleshian, A. M. & Sachs, F. Voltage-induced membrane movement. *Nature* **413,** 428–432 (2001).
6. Kim, G. H., Kosterin, P., Obaid, A. L. & Salzberg, B. M. A mechanical spike accompanies the action potential in mammalian nerve terminals. *Biophys. J.* **92,** 3122–3129 (2007).
7. Lin, Y. & Freund, L. B. Forced detachment of a vesicle in adhesive contact with a substrate. *Int. J. Solids Struct.* **44,** 1927–1938 (2007).
8. Matsuzaki, M., Honkura, N., Ellis-Davies, G. C. & Kasai, H. Structural basis of long-term potentiation in single dendritic spines. *Nature* **429,** 761–766 (2004).
9. Zheng, J. *et al.* Tensile regulation of axonal elongation and initiation. *J. Neurosci.* **11,** 1117–1125 (1991).
10. Hill, B. C., Schubert, E. D., Nokes, M. A. & Michelson, R. P. Laser interferometer measurement of changes in crayfish axon diameter concurrent with action potential. *Science* **196,** 426–428 (1977).
11. Iwasa, K., Tasaki, I. & Gibbons, R. C. Swelling of nerve fibers associated with action potentials. *Science* **210,** 338–339 (1980).
12. Terakawa, S. Changes in intracellular pressure in squid giant axons associated with production of action potentials. *Biochem. Biophys. Res. Commun.* **114,** 1006–1010 (1983).
13. Todorov, A. T., Petrov, A. G. & Fendler, J. H. Flexoelectricity of charged and dipolar bilayer-lipid membranes studied by stroboscopic interferometry. *Langmuir* **10,** 2344–2350 (1994).
14. Petrov, A. G., Miller, B. A., Hristova, K. & Usherwood, P. N. Flexoelectric effects in model and native membranes containing ion channels. *Eur. Biophys. J.* **22,** 289–300 (1993).
15. Nonnenmann, S. S., Leaffer, O. D., Gallo, E. M., Coster, M. T. & Spanier, J. E. Finite curvature-mediated ferroelectricity. *Nano Lett.* **10,** 542–546 (2010).
16. Breneman, K. D., Brownell, W. E. & Rabbitt, R. D. Hair cell bundles: flexoelectric motors of the inner ear. *PLoS ONE* **4,** e5201 (2009).
17. Harland, B., Brownell, W. E., Spector, A. A. & Sun, S. X. Voltage-induced bending and electromechanical coupling in lipid bilayers. *Phys. Rev. E* **81,** 031907 (2010).
18. Guck, J. *et al.* The optical stretcher: a novel laser tool to micromanipulate cells. *Biophys. J.* **81,** 767–784 (2001).
19. Brownell, W. E., Qian, F. & Anvari, B. Cell membrane tethers generate mechanical force in response to electrical stimulation. *Biophys. J.* **99,** 845–852 (2010).
20. Bausch, A. R., Ziemann, F., Boulbitch, A. A., Jacobson, K. & Sackmann, E. Local measurements of viscoelastic parameters of adherent cell surfaces by magnetic bead microrheometry. *Biophys. J.* **75,** 2038–2049 (1998).
21. Fu, J. *et al.* Mechanical regulation of cell function with geometrically modulated elastomeric substrates. *Nature Methods* **7,** 733–736 (2010).
22. Cohen-Karni, T., Qing, Q., Li, Q., Fang, Y. & Lieber, C. M. Graphene and nanowire transistors for cellular interfaces and electrical recording. *Nano Lett.* **10,** 1098–1102 (2010).
23. Shalek, A. K. *et al.* Vertical silicon nanowires as a universal platform for delivering biomolecules into living cells. *Proc. Natl Acad. Sci. USA* **107,** 1870–1875 (2010).
24. Xie, C. *et al.* Noninvasive neuron pinning with nanopillar arrays. *Nano Lett.* **10,** 4020–4024 (2010).
25. Hallstrom, W. *et al.* Fifteen-piconewton force detection from neural growth cones using nanowire arrays. *Nano Lett.* **10,** 782–787 (2010).

26. Nguyen, T. D. *et al.* Wafer-scale nanopatterning and translation into high-performance piezoelectric nanowires. *Nano Lett.* **10,** 4595–4599 (2010).
27. Qi, Y. *et al.* Piezoelectric ribbons printed onto rubber for flexible energy conversion. *Nano Lett.* **10,** 524–528 (2010).
28. Xu, S., Hansen, B. J. & Wang, Z. L. Piezoelectric-nanowire-enabled power source for driving wireless microelectronics. *Nature Commun.* **1,** 93 (2010).
29. Greene, L. A. & Tischler, A. S. Establishment of a noradrenergic clonal line of rat adrenal pheochromocytoma cells which respond to nerve growth-factor. *Proc. Natl Acad. Sci. USA* **73,** 2424–2428 (1976).
30. Stauffer, E. K. & Ziegler, R. J. Loss of functional voltage-gated sodium channels in persistent mumps virus-infected PC12 cells. *J. Gen. Virol.* **70,** 749–754 (1989).
31. Duval, F. F. C. *et al.* Characterisation of PZT thin film micro-actuators using a silicon micro-force sensor. *Sens. Actuat. A* **133,** 35–44 (2007).
32. Mosbacher, J., Langer, M., Horber, J. K. & Sachs, F. Voltage-dependent membrane displacements measured by atomic force microscopy. *J. Gen. Physiol.* **111,** 65–74 (1998).
33. Qi, Y. *et al.* Enhanced piezoelectricity and stretchability in energy harvesting devices fabricated from buckled PZT ribbons. *Nano Lett.* **11,** 1331–1336 (2011).
34. Feng, X. *et al.* Stretchable ferroelectric nanoribbons with wavy configurations on elastomeric substrates. *ACS Nano* **5,** 3326–3332 (2011).
35. Li, Z., Zhu, G., Yang, R., Wang, A. C. & Wang, Z. L. Muscle-driven *in vivo* nanogenerator. *Adv. Mater.* **22,** 2534–2537 (2010).

Acknowledgements

Author contributions

T.D.N., J.M.N. and M.C.M. devised the studies. T.D.N., N.D., J.M.N., M.J.B. and M.C.M. designed the experiments. T.D.N., N.D. and T.K. performed the experiments. P.K.P. developed the theoretical model. T.D.N., N.D., J.M.N., T.K., P.K.P., M.J.B. and M.C.M. wrote the paper.

Additional information

The authors declare no competing financial interests. Supplementary information accompanies this paper at www.nature.com/naturenanotechnology. Reprints and permission information is available online at http://www.nature.com/reprints. Correspondence and requests for materials should be addressed to M.C.M.

In our experiments the cells are patch clamped to induce depolarization and they rest on PZT nanobeams so that a change in radius of the cell causes a deflection of the beam, which in turn can be easily detected because the piezoelectric properties of PZT lead to the generation of a voltage upon bending. Our goal is to analyze these experiements so as to be able to predict the change in shape of the cells in response to membrane depolarization.

Model for voltage dependent membrane tension

The surface tension σ in a single leaflet of lipid bilayer membrane is controlled by the Lippmann equation which dictates that

$$\sigma = \sigma_0 - \frac{1}{2}C_D V_s^2, \tag{1}$$

where σ_0 is the voltage independent tension, C_D is the specific capacitance of the electric double layer (or cloud of ions) next to the leaflet, and V_s is the surface potential at the leaflet [S1]. This surface potential and the distribution of ions in the electric double layer is governed by the Poisson-Boltzmann equation [S2]. From the solution to the fully non-linear Poisson-Boltzmann equation near a surface with charge density q it can be shown that

$$V_s = \frac{2k_B T}{e} \sinh^{-1}\left(\frac{q}{2\sqrt{2c\epsilon_w \epsilon_0 k_B T}}\right), \tag{2}$$

where c is the ionic strength of the solution far away from the surface, ϵ_w is the relative perimittivity of water, ϵ_0 is the permittivity of vaccuum and $k_B T$ is the thermal energy scale and we have assumed that both positive and negative ions of valence 1 are present in the solution. This equation and (1) can then be applied to both the interior and exterior leaflets of the membrane and the surface tension in both can be added to give the surface tension τ in the cell-membrane. The result is:

$$\frac{(\tau - \tau_I)e}{\sqrt{(2k_B T)^3 \epsilon_w \epsilon_0}} = \sqrt{c_{ext}}\left[\sinh^{-1}\left(\frac{q_{ext} - C_m V}{2\sqrt{2c_{ext}\epsilon_w \epsilon_0 k_B T}}\right)\right]^2 + \sqrt{c_{int}}\left[\sinh^{-1}\left(\frac{q_{int} + C_m V}{2\sqrt{2c_{int}\epsilon_w \epsilon_0 k_B T}}\right)\right]^2, \tag{3}$$

where C_m is the capacitance of the lipid bilayer (assumed much larger than C_D on both the interior and exterior), V is the applied potential through the patch clamp and τ_I is a voltage independent tension. q_{int} and q_{ext} are the charge densities on the interior and exterior leaflets of the cell membrane and have to be treated as fitting parameters along with C_m and τ_I. But, appropriate values for these parameters are available from earlier work [S1].

Using the Young-Laplace law

In this section we will assume for simplicity that the cell remains spherical and demonstrate how a change in voltage through the patch-clamp results in a force exerted by the cell on
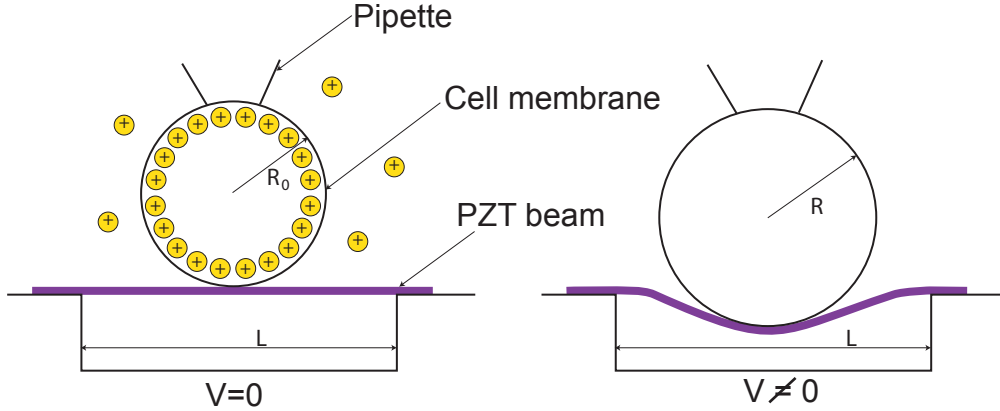
Figure 1: A cell 'patch-clamped' using a pipette. The potential difference between the interior and exterior of the cell can be changed using the patch clamp technique. There are ions both inside and outside the cell as shown in the left panel. The ions interact with opposite charges on the membrane and with each other to induce a tension in the membrane. The membrane tension can be changed by artificially changing the potential difference between the inside and outside of the cell. This causes a change in shape of the cell which can be detected by the deflection of the PZT beam as shown in the right panel. Here we assume for simplicity that the cell remains spherical. The more realistic case is treated later.

the substrate. Once the surface tension τ in the cell membrane is known in terms of the applied voltage V we can apply the Young-Laplace law to calculate how its shape changes. This law states that the pressure difference p between the interior and exterior of the cell is related to the surface tension and local mean curvature on the cell membrane through

$$p = \tau \left(\frac{1}{R_m} + \frac{1}{R_p} \right), \tag{4}$$

where R_m is the meridional (principal) curvature and R_p is the principal curvature along lines perpendicular to the meridians. We have, of course, assumed here that the cell membrane has an axisymmetric shape, which is good for the geometry of our experiments. Note that p remains constant even though the cell shape changes since the concentrations c_{int} and c_{ext} of ions are realistically assumed not to change when the cell is electrically and mechanically manipulated since they are controlled by regulation of ion channels by the cell. The Young-Laplace law (which is a statement of local mechanical equilibrium) and the boundary conditions imposed by the pipette and the PZT beam are sufficient to calculate the shape of the cell for some applied voltage V. The final expressions for the shape of the cell are in terms of elliptic functions as shown by Lin and Freund [S3] in a different context.

In order to illustrate how the general framework given above can be applied we will illustrate it by assuming that the cell remains spherical even after the tension in the cell membrane changes (see figure 1). Let us assume that at the resting state of a cell when $V = 0$ the membrane tension is τ_0, the radius of the cell is R_0 and the pressure difference is p. Then the Young-Laplace law gives $\frac{2\tau_0}{R_0} = p$. When $V \neq 0$ the cell's radius changes to R and the tension τ is given by eqn.(3). The PZT beam deflects by an amount $\delta = 2(R - R_0)$

9

at the center. This provides a reaction $F = k\delta$ where k is a spring constant. For instance, $k = \frac{192EI}{L^3}$ for a clamped-clamped beam and $k = \frac{48EI}{L^3}$ for a hinged-hinged beam, where E is the Young's modulus of PZT, I is the moment of inertia of the cross-section of the PZT beam, and L is its length. Realistically, k should be determined from experiment since we expect manufacturing defects in the PZT beam that would result in $\frac{48EI}{L^3} \leq k \leq \frac{192EI}{L^3}$. Mechanical equilibrium at the equator of the spherical cell demands that

$$\frac{2\tau}{R} + \frac{F}{\pi R^2} = p = \frac{2\tau_0}{R_0}. \tag{5}$$

This equation can be solved immediately to give

$$R = R_0 \left[\frac{\tau}{2\tau_0} + \frac{k}{2\pi\tau_0} + \sqrt{\left(\frac{\tau}{2\tau_0} + \frac{k}{2\pi\tau_0}\right)^2 - \frac{k}{\pi\tau_0}} \right]. \tag{6}$$

This formula provides a good estimate of the actual radius of the cell in the limit when k is small. Clearly, when $k = 0$, meaning the PZT beam is absent, the Young-Laplace result is recovered. The force F exerted by the cell on the PZT beam due to the change in voltage V can be computed using $F = 2k(R - R_0)$. When k is large we have to resort to a more general method explained in the following.

Analysis of cells on stiff PZT beams
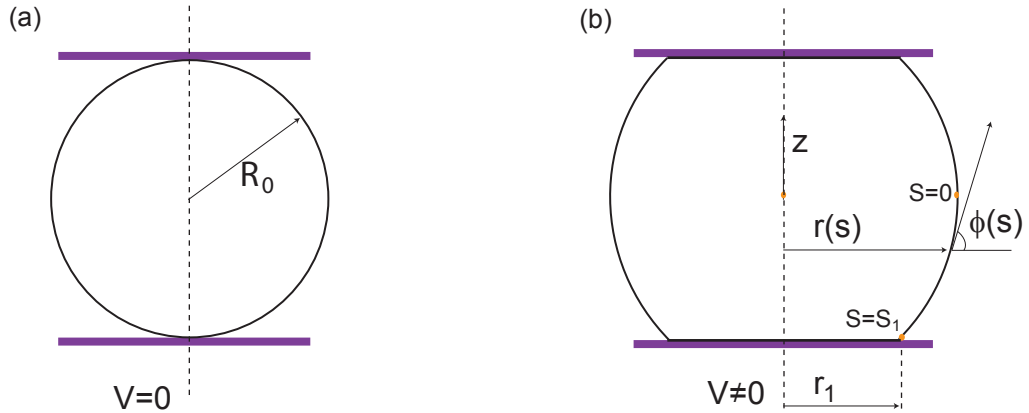
Figure 2: (a) Schematic diagram with the pipette and PZT beam replaced by planes. We assume that the pipette does not move and the PZT beam is much stiffer than the cell. The response of the cell resembles converse flexoelectricity – a potential difference causes a change in curvature of the cell membrane. (b) The change in membrane curvature causes a change in the shape of the cell. We assume that it remains axisymmetric about the vertical dashed line. The geometrical variables are indicated.

When the PZT beam on which the cell rests is stiff then it does not deflect much in response to the depolarization. We approximate the PZT beam as being infinitely stiff and

directly compute the reaction force imposed by the beam on the cell. Let this force be F. Then if we make a cut perpendicular to the axis of the cell where the radius is $r(s)$ and the tangent angle to the contour of the axisymmetric shape is $\phi(s)$ (see figure 2) then equilibrium demands that

$$2\pi\tau r(s)\sin\phi(s) = \pi r^2(s)p - F. \tag{7}$$

We want to know F and $r(s)$ as a function of τ. When $\tau = \tau_0$, $F = 0$ and the cell is a sphere of radius R_0, so that by applying the above equation at the equator where $\phi = \frac{\pi}{2}$ we see that

$$p = \frac{2\tau_0}{R_0}. \tag{8}$$

When $\tau > \tau_0$ the cell tends to bulge but we will assume that the distance $2R_0$ between the pipette and the PZT beam changes by a negligible amount. This constraint is enforced by a force $F \neq 0$. In the experiments $2R_0$ is about $20\mu m$ and it changes by only a few nanometers when the cells are depolarized. So, our assumption that the distance between the pipette and the PZT beam does not change is justified. When $F \neq 0$ the cell is squished and it makes contact with the PZT beam over a circular region of radius r_1. The angle ϕ_1 at $r = r_1$ depends on the adhesion energy per unit area between the cell and the PZT beam. If the adhesion energy density is zero then the angle ϕ_1 is zero too. So, we have

$$\sin\phi_1 = \frac{pr_1}{2\tau} - \frac{F}{2\pi r_1\tau} = 0 \tag{9}$$

which gives $r_1^2 = \frac{F}{\pi p}$. From geometry,

$$\frac{dr}{ds} = \cos\phi(s) = \sqrt{1 - \sin^2\phi(s)}, \qquad \frac{dz}{ds} = \sin\phi(s) \tag{10}$$

where $\sin\phi(s)$ is given by (7) in terms of $r(s)$ and F. We can therefore integrate the differential equation for $r(s)$ and get

$$r(s) = \frac{\sqrt{2}\tau}{p}\sqrt{1 + \frac{Fp}{2\pi\tau^2} + \sqrt{1 + \frac{Fp}{\pi\tau^2}}\cos\frac{ps}{\tau}}, \tag{11}$$

where $s = 0$ is taken to be at the equator of the cell. Let $s = s_1$ be such that $r(s_1) = r_1$ and $\phi(s_1) = \phi_1 = 0$. Using $r_1^2 = F/\pi p$ and (11) above it is easy to see that

$$\cos\frac{ps_1}{\tau} = \frac{-1}{\sqrt{1 + \frac{Fp}{\pi\tau^2}}}, \tag{12}$$

from which we get

$$s_1 = \frac{\tau}{p}\left(\pi + \cos^{-1}\frac{1}{\sqrt{1 + \frac{Fp}{\pi\tau^2}}}\right). \tag{13}$$

Integrating the equation for $z(s)$ we get

$$z(s) = \int_0^s \sin\phi(s)\,ds = \int_0^s\left(\frac{pr(s)}{2\tau} - \frac{F}{2\pi\tau r(s)}\right), \tag{14}$$

11

where $r(s)$ is given by (11) above. We substitute for $r(s)$ to get

$$z(s) = \frac{1}{\sqrt{2}} \int_0^s \sqrt{1 + \frac{Fp}{2\pi\tau^2} + \sqrt{1 + \frac{Fp}{\pi\tau^2}} - 2\sqrt{1 + \frac{Fp}{\pi\tau^2}} \sin^2 \frac{ps}{2\tau}} \, ds$$
$$- \frac{Fp}{2\sqrt{2}\pi\tau^2} \int_0^s \frac{ds}{\sqrt{1 + \frac{Fp}{2\pi\tau^2} + \sqrt{1 + \frac{Fp}{\pi\tau^2}} - 2\sqrt{1 + \frac{Fp}{\pi\tau^2}} \sin^2 \frac{ps}{2\tau}}}. \tag{15}$$

We take $s = s_1$ and reduce this expression to

$$z(s_1) = \frac{\tau}{p}\left(1 + \sqrt{1 + \frac{Fp}{\pi\tau^2}}\right) \int_0^{\frac{ps_1}{2\tau}} \sqrt{1 - m^2 \sin^2 \theta} \, d\theta - \frac{F}{\pi\tau} \frac{1}{1 + \sqrt{1 + \frac{Fp}{\pi\tau^2}}} \int_0^{\frac{ps_1}{2\tau}} \frac{d\theta}{\sqrt{1 - m^2 \sin^2 \theta}}, \tag{16}$$

where

$$m^2 = \frac{2\sqrt{1 + \frac{Fp}{\pi\tau^2}}}{1 + \frac{Fp}{2\pi\tau^2} + \sqrt{1 + \frac{Fp}{\pi\tau^2}}} \leq 1, \tag{17}$$

and θ is a dummy variable. Recognizing the incomplete elliptic integrals above we write

$$z(s_1) = \frac{\tau}{p}\left(1 + \sqrt{1 + \frac{Fp}{\pi\tau^2}}\right) E(\theta_1|m) - \frac{F}{\pi\tau} \frac{1}{1 + \sqrt{1 + \frac{Fp}{\pi\tau^2}}} F(\theta_1|m), \tag{18}$$

where $E(x|k)$ is the incomplete elliptic integral of the second kind with modulus k and $F(x|k)$ is the incomplete elliptic integral of the first kind with modulus k and $\theta_1 = \frac{ps_1}{2\tau}$. The stiff PZT beams enforce the constraint that $z(s_1) = R_0$. For small values of $\frac{Fp}{\pi\tau^2}$ we see from (13) and (17) that $\theta_1 \approx \frac{\pi}{2}$ and $m^2 \approx 1$. Under these circumstances the second term involving $F(\theta_1|m)$ is much smaller than the first term involving $E(\theta_1|m)$, so we neglect the second term. Furthermore, $E(\theta_1|1) = \sin \theta_1$. We note that

$$\theta_1 = \frac{ps_1}{2\tau} = \frac{\pi}{2} + \frac{1}{2}\cos^{-1}\frac{1}{\sqrt{1+y}}, \qquad y = \frac{Fp}{\pi\tau^2} << 1. \tag{19}$$

So (18) becomes

$$\frac{pR_0}{\tau} \approx \left(1 + \sqrt{1+y}\right)\sqrt{\frac{1 + \frac{1}{\sqrt{1+y}}}{2}}, \qquad y << 1. \tag{20}$$

Expanding upto linear order in y we are left with

$$1 + \frac{y}{8} = \frac{pR_0}{2\tau}, \tag{21}$$

which can be solved to get

$$y = \frac{Fp}{\pi\tau^2} = -8\left(1 - \frac{pR_0}{2\tau}\right). \tag{22}$$

This gives the force exerted by the beam on the cell. The final formula for the force exerted by the *cell on the beam* is (note the change in sign of F):

$$F = \frac{8\pi\tau^2}{p}\left(1 - \frac{R_0}{R}\right), \tag{23}$$

where

$$p = \frac{2\tau_0}{R_0}, \qquad R = \frac{2\tau}{p}, \tag{24}$$

and τ is given by (3). Clearly, $F > 0$ when $R > R_0$.

Pancake shaped cell

Cells on many substrates become pancake shaped. This suggests that there is an adhesive interaction between the cell and the substrate that results in a decrease of free energy by amount Γ per unit contact area. To account for the adhesive interactions we have to make some non-trivial modifications to the theory given in the previous section. The shape of the cell is still described by the same equation for $r(s)$ (eqn. (11)). But, the expression for s_1 becomes more complicated:

$$\cos\frac{ps_1}{\tau} = \frac{\frac{p^2 r_1^2}{2\tau^2} - 1 - \frac{Fp}{2\pi\tau^2}}{\sqrt{1 + \frac{Fp}{\pi\tau^2}}}. \tag{25}$$

Here r_1 is the radius over which contact occurs between the cell and the substrate and it is no longer zero when $F = 0$ because of the adhesive interactions. The integral for $z(s)$ remains the same but $\frac{ps_1}{2\tau}$ appears in the limit of the integral where the expression for calculating s_1 is given above. The analysis to impose the constraint that the cell is confined between two fixed surfaces proceeds along the same lines as in the previous section. If the distance between the two confining surfaces is $2Z_0$ (see figure 3) then the equation to solve for F takes the form

$$Z_0 = \frac{\tau}{p}\left[1 + \sqrt{1 + \frac{Fp}{\pi\tau^2}}\right]\sin\frac{ps_1}{2\tau} = \frac{\tau}{p}\left[1 + \sqrt{1 + \frac{Fp}{\pi\tau^2}}\right]\sqrt{\frac{1 - \cos\frac{ps_1}{\tau}}{2}}, \tag{26}$$

where we can use (25) for $\cos\frac{ps_1}{\tau}$. When $\tau = \tau_0$, $F = 0$ and $r_1 = r_0$ the above equation yields

$$Z_0 = \frac{2\tau_0}{p}\sqrt{1 - \frac{pr_0^2}{4\tau_0^2}}. \tag{27}$$

Note that if $r_0 = 0$ when $\tau = \tau_0$ and $F = 0$ then the cell is a sphere and $Z_0 = R_0 = \frac{2\tau_0}{p}$, as expected. This is the case when $\Gamma = 0$. When $\Gamma \neq 0$ we have to determine the magnitude of Γ from the known pancake shape of the cell when $F = 0$. This is a difficult exercise in general, but in a certain limit it is possible to write some simple relations [S3]. In particular, the radius r_1 over which contact between the cell and the substrate occurs in this limit is given by [S3]:

$$r_1 = \frac{\Gamma}{p}\left[\sqrt{\frac{pR_0}{\Gamma} - \frac{F}{\pi R_0\Gamma} - 1} + \sqrt{\frac{pR_0}{\Gamma} - \frac{F}{\pi R_0\Gamma} + \frac{Fp}{\pi\Gamma^2} - 1}\right]. \tag{28}$$

When $F = 0$ and $\tau = \tau_0$ this reduces to

$$r_0 = \frac{2\Gamma}{p}\sqrt{\frac{pR_0}{\Gamma} - 1}, \tag{29}$$
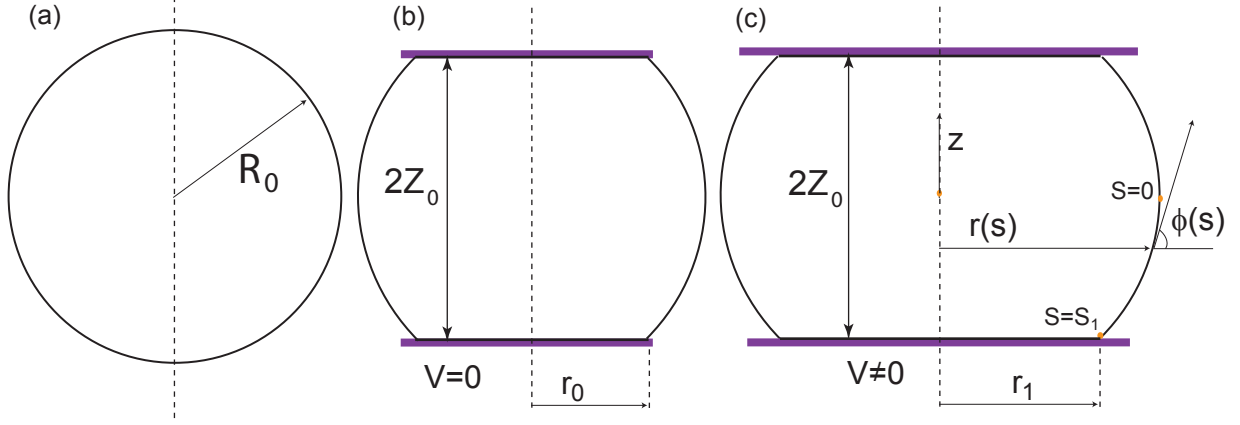
Figure 3: (a) The cell is a sphere of radius R_0 when it is not in contact with a substrate. (b) When it is brought in contact with a substrate at the top and bottom it becomes pancake shaped due to adhesive interactions. The geometry of the pancake is characterized by Z_0 and r_0, both of which depend on R_0 and the adhesion energy density Γ. (c) The force exerted by the cell on the substrate when $V \neq 0$ is determined by enforcing the constraint that Z_0 remains fixed even though the contact radius r_1 changes.

where $p = \frac{2\tau_0}{R_0}$. If we know τ_0, R_0, and r_0 then the parameter Γ can be estimated. Then Z_0 can be calculated from (27) and we can solve for F from (26). After carrying out these calculations we find that the equation for F is

$$Z_0 = R_0(1 - \frac{\Gamma}{\tau_0}) = \frac{\tau}{p}\left[\frac{1 + \sqrt{1 + \frac{Fp}{\pi\tau^2}}}{\sqrt{2}}\right]\left[1 - \frac{\frac{p^2 r_1^2}{2\tau^2} - 1 - \frac{Fp}{2\pi\tau^2}}{\sqrt{1 + \frac{Fp}{\pi\tau^2}}}\right]^{1/2}. \tag{30}$$

We can solve this equation for F using Newton's method. Unfortunately, a simple solution like the one in the previous section is difficult to obtain. In figure 4 we have plotted the solution for F using $R_0 = 10\mu m$ and $r_0 = 0.85R_0$. It fits the data quite well and corresponds to $\frac{\Gamma}{pR_0} \approx 0.23$ which is in the regime where (28) is valid.

Cell off-center on the PZT beam

The cell contacts the PZT beam over a circular patch of radius r_1. Let us assume for simplicity that $r_1 << L$ where L is the length of the beam. In that case we can assume that the cell is exerting a point force F on the beam. Let this point force F act at $x = x_0$ with $0 < x_0 < L$ (see figure 5(a)). If the beam is clamped at both ends this leads to a deflection profile:

$$y(x|x_0) = \frac{F}{6EI}(1 - \frac{x_0}{L})^2\left[x^3(1 + \frac{2x_0}{L}) - 3x_0 x^2\right] - \frac{F}{6EI}\langle x - x_0\rangle^3, \tag{31}$$

$$\frac{dy}{dx} = \frac{F}{2EI}(1 - \frac{x_0}{L})^2\left[x^2(1 + \frac{2x_0}{L}) - 2x_0 x\right] - \frac{F}{2EI}\langle x - x_0\rangle^2. \tag{32}$$

14
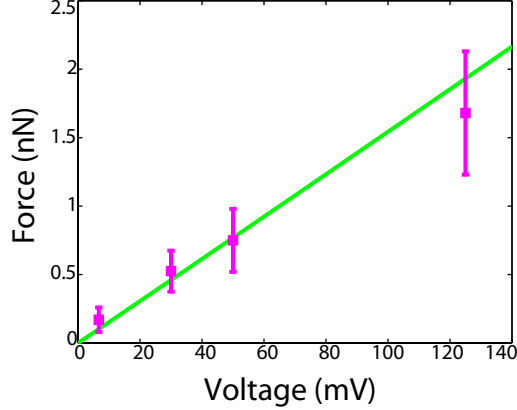
Figure 4: The experimental data (pink points) can be fit by theory even if we start with a pancake shaped cell. For this plot we have taken $R_0 = 10\mu$m and $r_0 = 0.85R_0$.

where $\langle x - x_0 \rangle^n = 0$, if $x < x_0$ and $\langle x - x_0 \rangle^n = (x - x_0)^n$, if $x \geq x_0$. The deflection $y(x_0|x_0)$ right under the load is given by

$$y(x_0|x_0) = -\frac{F}{3EIL^3}\left[x_0(L - x_0)\right]^3.$$

(33)

This deflection is zero when $x_0 = 0, L$ and maximum when $x_0 = \frac{L}{2}$. For a given F, if $x_0 = \frac{L}{2}$ the deflection $y(\frac{L}{2})$ is given by

$$y(\frac{L}{2}) = -\frac{FL^3}{192EI}.$$

(34)

We can now compute the ratio $\frac{y(x_0)}{y(\frac{L}{2})}$ as follows:

$$\frac{y(x_0|x_0)}{y(\frac{L}{2}|\frac{L}{2})} = 64\left[\frac{x_0}{L}(1 - \frac{x_0}{L})\right]^3.$$

(35)

In our experiments the PZT beams are calibrated so that a measured voltage gives us the force exerted by the cell on the PZT beam assuming that the cell is at $x = \frac{L}{2}$. If the cell is not at the center of the beam then the deflection of the beam will be smaller and the apparent force $F_{app} = \frac{192EIy(x_0|x_0)}{L^3}$. This is related to the actual F exerted by the cell as follows:

$$\frac{F_{app}}{F} = \frac{y(x_0|x_0)}{y(\frac{L}{2}|\frac{L}{2})} = 64\left[\frac{x_0}{L}(1 - \frac{x_0}{L})\right]^3.$$

(36)

E, I and L for the PZT beams are known but the deflections $y(x)$ are too small to measure accurately. The voltages produced by the beam deflections, however, can be accurately measured and give us F_{app}.

Let us now consider the case when the load F is not a point load but is distributed over a length $2z$ along the beam and centered at x_0. The load is uniformly distributed with intensity q, so that $2qz = F$ as shown in figure 5(b). In this case the deflection profile is

15

given by:

$$y(x|x_0, z) = \frac{2qzx^3}{EIL}\left[(1 - \frac{x_0}{L})^2(\frac{L}{2} + x_0) - \frac{z^2}{L^2}(\frac{L}{2} - x_0)\right] + \frac{qzx^2}{EIL}\left[z^2(\frac{2}{3} - \frac{x_0}{L}) - \frac{x_0}{L}(L - x_0)^2\right]$$
$$- \frac{q}{24EI}\langle x - x_0 + z\rangle^4 + \frac{q}{24EI}\langle x - x_0 - z\rangle^4. \tag{37}$$

Evaluating the deflection at the center point of the distributed load x_0, we get

$$y(x_0|x_0, z) = \frac{2qzx_0^2}{3EIL}(L - x_0)^2\left[\frac{z^2}{L^2} - \frac{x_0}{L}(1 - \frac{x_0}{L})\right] - \frac{qz^4}{24EI}. \tag{38}$$

Note that as $z \to 0$ with $2qz = F$ we recover (33). To get an idea of how the distributed
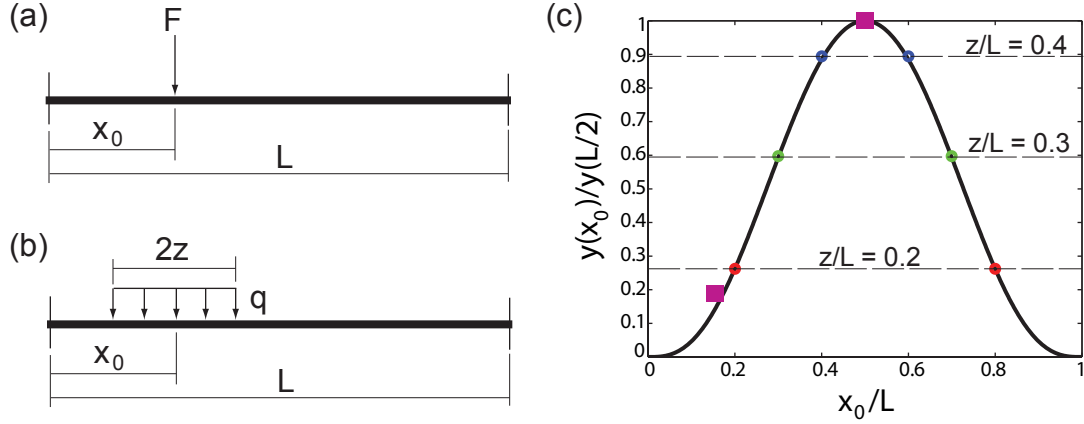
Figure 5: A cell exerts a distributed load q on a beam over a region of length $2z$ as shown in (b) with $2qz = F$. The center point of the distributed load is at x_0. $z = 0$ corresponds to a point load on the beam as shown in (a). We wish to compute the ratio of deflections $\frac{y(x_0)}{y(\frac{L}{2})}$ as a function of z and x_0. This is plotted in (c). The black curve corresponds to $z = 0$. For $z \neq 0$ the curve remains the same but the range over which $\frac{y(x_0)}{y(\frac{L}{2})}$ varies is smaller because the range of x_0 becomes $z \leq x_0 \leq L - z$. Using optical images we were able to observe a cell near $x/L = 0.15$ and another near $x/L = 0.5$. Recall that $\frac{y(x_0)}{y(\frac{L}{2})} = \frac{F_{app}}{F}$ from (36). For $x/L = 0.5$ we found $F_{app} = 1.7$nN and for $x/L = 0.15$ we got $F_{app} = 0.34$nN for the same amount of depolarization. These are plotted as magenta squares in (c) assuming $F = 1.7$nN. The point corresponding to $x/L = 0.15$ lies close to the theoretical curve.

load affects the deflection let us compute the ratio $\frac{y(x_0|x_0,z)}{y(\frac{L}{2}|\frac{L}{2},z)}$ which we will call $\frac{y(x_0)}{y(\frac{L}{2})}$ for compactness. This is given by

$$\frac{y(x_0|x_0, z)}{y(\frac{L}{2}|\frac{L}{2}, z)} = \frac{16\left[\frac{x_0}{L}(1 - \frac{x_0}{L})\right]^2\left[\frac{z^2}{L^2} - \frac{x_0}{L}(1 - \frac{x_0}{L})\right] - \frac{z^3}{L^3}}{\left[\frac{z^2}{L^2} - \frac{1}{4}\right] - \frac{z^3}{L^3}} = \frac{y(x_0)}{y(\frac{L}{2})}. \tag{39}$$

This expression is plotted for $z = 0$ (corresponding to a point force) in figure 5(c) as the black curve. The range for $\frac{y(x_0)}{y(\frac{L}{2})}$ is $0 \leq \frac{y(x_0)}{y(\frac{L}{2})} \leq 1.0$ when $z = 0$. If the point of application of F is nearer to the ends than to the center then the deflection at x_0 is lesser than

16

what it would be if F was acting at $\frac{L}{2}$. If $z \neq 0$ (corresponding to a distributed load q over a region $2z$) then the range for x_0 becomes $z \leq x_0 \leq L - z$ but the curve does not change. So, the conclusion that the beam deflection is maximum when $x_0 = \frac{L}{2}$ does not change. But, the range over which the deflection at x_0 varies decreases as z increases. In figure 5(c) the range for $\frac{y(x_0)}{y(\frac{L}{2})}$ is above the dashed horizontal line labeled $z/L = 0.3$ when $z = 0.3L - 0.6 \leq \frac{y(x_0)}{y(\frac{L}{2})} \leq 1.0$. This means that the error in computing the force exerted by the cell by just looking at the deflection at the center of the beam decreases as z increases.

References

[S1] Zhang, P.-C., Keleshian, A. M. and Sachs, F. Voltage-induced membrane movement. *Nature* **413**, 428-432, (2001).

[S2] Boal, D. H. *Mechanics of the cell*, Cambridge University Press, (2001).

[S3] Lin, Y. and Freund, L. B. Forced detachment of a vesicle in adhesive contact with a substrate. *Intl. J. Solids Struc.* **44**, 1927-1938, (2007).